

Unsupervised Discovery of Non-Linear Plasma Physics using Differentiable Kinetic Simulations

A. S. Joglekar

Ergodic LLC, San Francisco, CA 94117, USA and

*Department of Nuclear Engineering and Radiological Sciences,
University of Michigan, Ann Arbor, MI 48109, USA*

A. G. R. Thomas

*Department of Nuclear Engineering and Radiological Sciences,
University of Michigan, Ann Arbor, MI 48109, USA*

Abstract

Plasma supports collective modes and particle-wave interactions that leads to complex behavior in, for example, inertial fusion energy applications. While plasma can sometimes be modeled as a charged fluid, a kinetic description is often crucial for studying nonlinear effects in the higher dimensional momentum-position phase-space that describes the full complexity of plasma dynamics. We create a differentiable solver for the 3D partial-differential-equation describing the plasma kinetics and introduce a domain-specific objective function. Using this framework, we perform gradient-based optimization of neural networks that provide forcing function parameters to the differentiable solver given a set of initial conditions. We apply this to an inertial-fusion relevant configuration and find that the optimization process exploits a novel physical effect.

I. INTRODUCTION

Kinetic plasma physics is described, typically, using various formulations or realizations of Boltzmann-like transport equations for the electron and ion species. A special case that is frequently studied is that of dynamics restricted to one spatial dimension and one momentum dimension ('1D-1V') for a single species of particles, given by

$$\frac{\partial f}{\partial t} + v \frac{\partial f}{\partial x} - E \frac{\partial f}{\partial v} = \left[\frac{\delta f}{\delta t} \right]_{coll}, \quad (1)$$

where the electric field is $E(x, t) = \int f \, dv - 1$, and the particle distribution function is $f = f(t, x, v)$. The left-hand side of this equation describes the evolution of the particle distribution in 'macroscopic' field E that arises self-consistently from the one-particle distribution f . The right-hand side provides a description of two-particle and higher correlations (i.e. collisions). Equation 1, along with Gauss's Law along with a particular form of the collision operator for two-particle interactions, is often termed the Vlasov-Poisson-Fokker-Planck (VPFP) equation set. Solving the VPFP set is often analytically intractable, even in 1D-1V. This is because the left-hand-side has a stiff linear transport term, has a non-linear term in $E \partial f / \partial v$, and can sustain wave propagation and other hyperbolic partial-differential-equation (PDE) behavior. Additionally, the right hand side is typically represented by a hyperbolic, advection-diffusion, partial-differential-equation. Making progress on kinetic plasma physics requires computational simulation tools.

Numerical solutions to the 1D-1V VPFP equation set have been applied in research

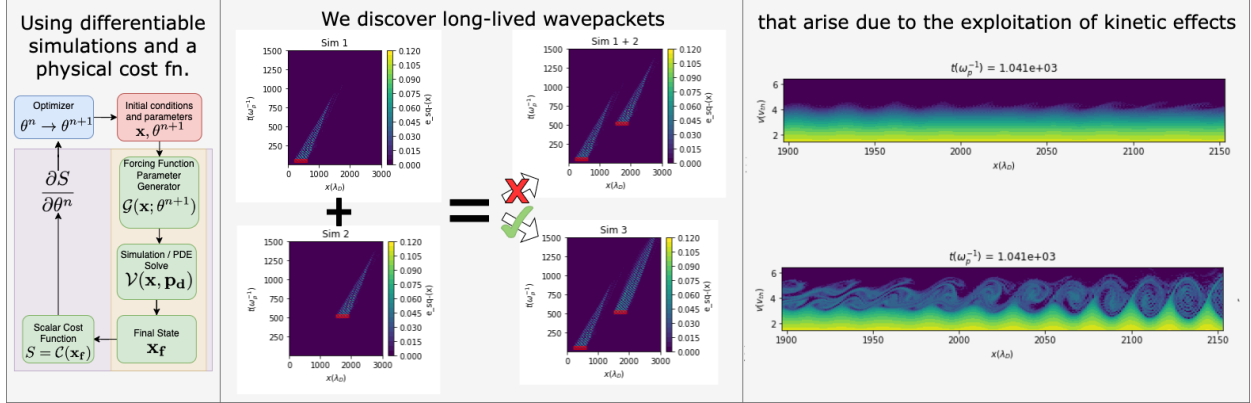


FIG. 1: **Left** - We create a differentiable loop to learn forcing function parameters that optimize for a free energy and entropy metric. **Middle** - The optimization uncovers a superadditive process that results in a long-lived second wavepacket. **Right** - Deeper inspection shows that the learning process exploits novel kinetic plasma physics in order to minimize damping, where the second wavepacket is able to leverage the electrons from the first wavepacket.

on laser-plasma interactions in the context of inertial fusion, for example in plasma-based accelerators ([1, 2]), space physics ([3]), fundamental plasma physics ([4]), and inertial fusion ([5, 6, 7]). Such numerical simulations may be used to explore initial conditions and forcing functions to understand the behavior of a physical effect in response to input parameters. Multi-dimensional ‘brute-force’ scans are, however, inefficient and costly and it is therefore beneficial to seek a more guided approach.

Differentiable simulations have been used in a variety of contexts for such guided searches, for example learning parameters for molecular dynamics ([8]), learning differencing stencils in PDEs ([9, 10, 11]), and controlling PDEs ([12]). In particular, there have been several recent applications of gradient-descent to fusion plasma physics. Analytic approaches have resulted in the development of adjoint methods for shape derivatives of functions that depend on magnetohydrodynamics (MHD) equilibria ([13, 14]). These methods have been used to perform optimization of stellarator design ([15]). In other work, by using gradients obtained from analytic ([16]) and automatic differentiation (AD) ([17]), the FOCUS and FOCUSADD codes optimize coil shape. These advances are founded on the concept of performing a sensitivity analysis towards device design. Here, we apply AD towards learning physical relationships and discovering novel phenomena in the VPFP dynamical system by training

neural networks through differentiable simulations that solve Eq. 1.

In this work, we extend previous findings of the etching of nonlinear plasma wavepackets by localized damping at the rear of the packet [6] in the context of inertial fusion to study the effect of the hot electrons from one wavepacket on upstream wavepackets using a gradient-based approach. We train a neural network that provides control parameters to the PDE solver. By choosing physical parameters as inputs and control parameters as outputs of the neural network, we enable the neural network to learn a function that describes the physical relationship between the plasma parameters and the forcing function parameters e.g. the resonance frequency. We train the neural network in an unsupervised fashion using a cost function based on the maximum entropy principle. This enables us to create self-learning plasma physics simulations, where the optimization process provides a physically interpretable function that can enable physics discovery.

II. PHYSICS DISCOVERY USING DIFFERENTIABLE SIMULATIONS

In this section, we provide a step-by-step description of how a traditional simulation-based computational physics workflow may be modified to perform closed-loop optimization.

A. Open Loop: Manual Workflow

Figure 2a depicts a typical workflow of a computational scientist represented as a cyclic graph. The scientist defines the parametric inputs that create the state vector \mathbf{x} . This can contain any parameters that are used to define the simulation e.g. the grid size, the number of solver steps, etc. For didactic purposes, the physical parameters to the simulation may be separated from \mathbf{x} into a different vector of inputs \mathbf{p}_d e.g. the forcing function parameters, the viscosity coefficient etc.

Each of \mathbf{x} and \mathbf{p}_d is passed to the algorithm that solves the PDE which is represented by the function, \mathcal{V} . The output of these simulations is stored in the final state vector \mathbf{x}_f . The final state is postprocessed using a domain-specific set of algorithms devised by the scientist or otherwise. The results of the postprocessing are interpreted by the scientist who then determines the next set of inputs and parameters.

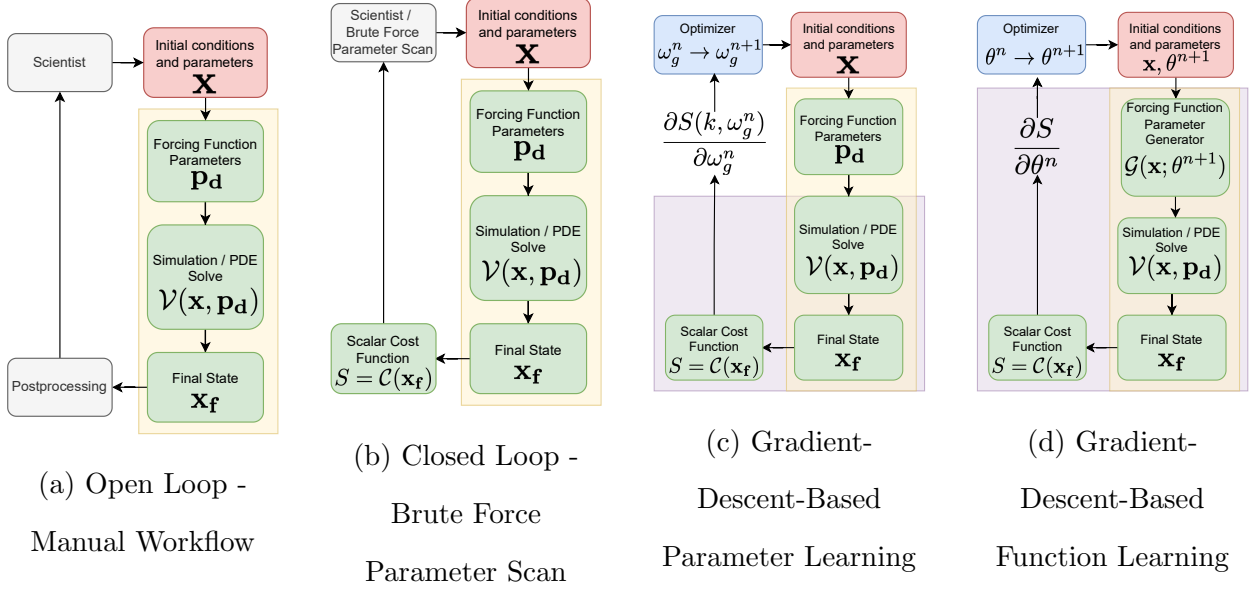


FIG. 2: (a) A typical workflow of a computational scientist where the scientist provides the initial conditions and forcing function parameters to a partial-differential-equation (PDE) solve. The output of the solve is stored as the final state \mathbf{x}_f . The final state is analyzed by the scientist using domain-specific postprocessing algorithms. (b) A cost function and a parameter scan is introduced which enables a closed-loop search. (c) A gradient-descent based optimization algorithm replaces the parameter-scan to provide a more efficient search mechanism. This requires the components in the purple background to be written in an auto-differentiable framework (d) We add a neural network that generates the forcing function parameters as a function of other parameters. This generalizes the learnings from (c) and enables interpolation and extrapolation within the learned parameters.

B. Closed Loop: Brute Force Parameter Scan

Figure 2b shows a more automated workflow. We replace the gray-box postprocessing step with the calculation of a scalar quantity S using a Cost Function \mathcal{C} on the final state \mathbf{x}_f . This reduces the complexity of the interpretation of the postprocessing and enables a more rapid search in parameter space. The decrease in required human effort for completing one cycle enables the scientist to execute this loop as a brute force parameter scan over a pre-defined parameter space. At the end, the scientist can look up the minimum/maximum of the scalar cost function, and find the parameters which provide that minimum.

The parameter scan approach scales with the number of different unique parameters and

the number of values of each parameter. e.g. a 2-D search in x and y requires $N_x \times N_y$ calculations. Therefore, the parameter scan approach quickly becomes inefficient when there are many parameters to scan, or when the required resolution in parameter space is very high. To search this parameter space efficiently, and to escape the linear scaling with each parameter, we can use gradient descent.

C. Gradient-Descent-Based Parameter Learning

Figure 2c includes two modifications. The scientist/parameter search graybox has been replaced with a gradient-descent-based optimization algorithm. This algorithm provides the updated parameters, e.g. ω_G , a guess for the resonant frequency of the system, for the next iteration of the loop. The gradient-descent algorithm requires the calculation of an accurate gradient.

Symbolic differentiation is out of the question here as we do not have an analytical form for our system. In the appendix, we compare the performance of Finite Differencing to acquire the gradient and confirm that Automatic Differentiation is a superior method for this purpose. Therefore, by writing our PDE solver \mathcal{V} and the cost function \mathcal{C} using a numerical framework that supports Automatic Differentiation, we are able to perform gradient-descent. Since

$$\mathcal{S} = \mathcal{C}(\mathbf{x}_f) = \mathcal{C}(\mathcal{V}(\mathbf{x}, \mathbf{p}_d)),$$

the gradient for the update-step is given by

$$\frac{\partial \mathcal{S}}{\partial \mathbf{p}_d} = \frac{\partial \mathcal{C}(\mathcal{V}(\mathbf{x}, \mathbf{p}_d))}{\partial \mathbf{p}_d} = \frac{\partial \mathcal{S}}{\partial \mathcal{V}} \frac{\partial \mathcal{V}}{\partial \mathbf{p}_d}.$$

For example, if we wish to learn the resonant frequency, ω , that optimizes for the scalar, \mathcal{S} , we compute

$$\frac{\partial \mathcal{S}}{\partial \omega} = \frac{\partial \mathcal{S}}{\partial \mathcal{V}} \frac{\partial \mathcal{V}}{\partial \omega}. \quad (2)$$

Assuming a well-behaved solution manifold, performing gradient-descent tends to reduce the number of iterations required to find the minimum in comparison to a evenly-spaced parameter scan, especially when the required resolution is unknown ([18]). Put another way, gradient-descent effectively provides an adaptive stepping mechanism in-lieu of the pre-defined values that represent a parameter scan.

D. Gradient-Descent-Based Function Learning

In the final step, we can replace the lookup-like capability of the parameter optimization and choose to learn a blackbox function that can do the same. Through that process, we also gain the ability to interpolate and extrapolate with respect to the input space.

Here, we choose to use neural networks, with a parameter vector θ , to represent the black box function. This allows us to extend the gradient-descent based methodology and leverage existing numerical software to implement this differentiable programming loop. Now,

$$\mathcal{S} = \mathcal{C}(\mathbf{x}_f) = \mathcal{C}(\mathcal{V}(\mathbf{x}, \mathbf{p}_d)) = \mathcal{C}(\mathcal{V}(\mathbf{x}, \mathcal{G}(\mathbf{x}, \mathbf{p}_d; \theta))),$$

where \mathcal{G} is a function that generates the desired forcing function parameter given a parameter vector θ . To extend the example from sec. II C, ω is now a function given by $\omega = \mathcal{G}(\mathbf{x}, \mathbf{p}_d; \theta)$.

We compute the same gradient as in eq. 2 and add a correction factor that arises because the parameter (vector) is now θ , rather than ω . The necessary gradient for the gradient update is now given by

$$\frac{\partial \mathcal{S}}{\partial \theta} = \left[\frac{\partial \mathcal{S}}{\partial \mathcal{V}} \frac{\partial \mathcal{V}}{\partial \mathcal{G}} \right] \frac{\partial \mathcal{G}(\mathbf{x}, \mathbf{p}_d; \theta)}{\partial \theta}. \quad (3)$$

III. DISCOVERY OF LONG-LIVED NONLINEAR PLASMA WAVEPACKETS

When electrostatic waves are driven to large amplitude, electrons can become trapped in the large potential ([19, 20]). Simulations of Stimulated Raman Scattering (SRS) in inertial confinement fusion (ICF) scenarios show that similar large-amplitude waves of finite extent are generated in the laser-plasma interaction, and that particle trapping is correlated with the transition to the high-reflectivity burst regime of SRS ([5, 21]).

Simulating wavepackets, similar to those generated in SRS, but in isolation, has illuminated kinetic dynamics where trapped electrons, with velocity $\approx v_{ph}$, transit the wavepacket which is moving at the slower group velocity v_g . The transit of the trapped electrons from the back of the wavepacket to the front results in the resumption of Landau damping at the back and the wavepacket is then damped away ([6]). Recent work ([22]) modeled the interaction of multiple speckles with a magnetic field acting as a control parameter. Since the effect of the magnetic field is to rotate the distribution in velocity space, the field strength serves as a parameter by which the authors control scattered particle propagation. Using

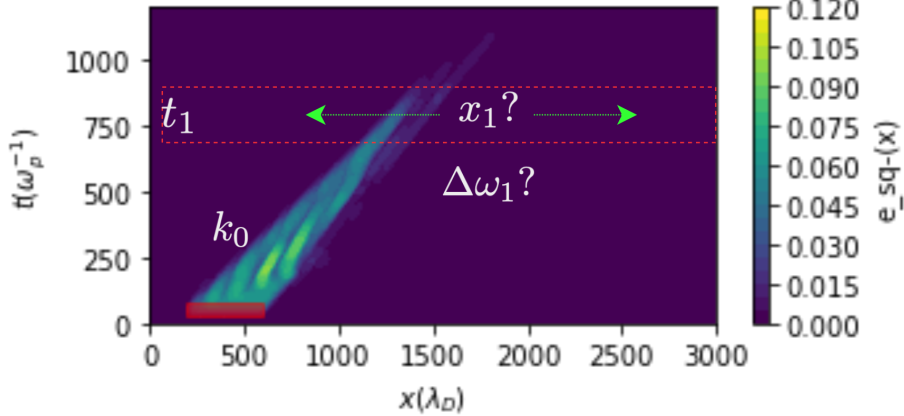


FIG. 3: Given a first wavepacket with wavenumber k_0 and a desired time of second wavepacket excitation t_1 , the task is to learn functions that give the optimal frequency ω_1 and spatial location x_1 of the second wavepacket.

this, along with carefully placed laser speckles, they show that scattered light and particles can serve as the trigger for SRS.

Here, we ask *What happens when a non-linear electron plasma wavepacket is driven on top of another?* To answer this question, we reframe it as an optimization problem and ask, *What is the best way to excite a wavepacket that interacts with a pre-existing wavepacket?*

We start with a large-amplitude, finite-length electrostatic wavepacket driven by a forcing function with parameters given by

$$\mathbf{p}_0 = [x_0, \omega_0, t_0, k_0], \quad (4)$$

where x_i is the location of excitation, ω_i is the frequency, t_i is the time of excitation, and k_i is the wavenumber, of the i^{th} wavepacket.

Since we seek to excite a second wavepacket that can interact with the detrapped electrons, we set the wavenumber $k_1 = k_0$. We reparameterize the resonant frequency, ω_1 , with a frequency shift, $\Delta\omega_1$ and the linear resonant frequency ω_0 such that $\omega_1 = \omega_0 + \Delta\omega_1$.

We use the time of excitation of the second wavepacket, t_1 , as an independent variable along with k_0 . For each t_1 and k_0 , we seek to learn functions that produce x_1 and $\Delta\omega_1$ i.e. we seek to learn $x_1(t_1, k_0)$ and $\Delta\omega_1(t_1, k_0)$. The entire parameter vector for the second wavepacket is given by

$$\mathbf{p}_0 = [x_1(t_1, k_0), \Delta\omega_1(t_1, k_0), t_1, k_0]. \quad (5)$$

This framing is also illustrated in fig. 3 where given k_0 and t_1 , we seek functions for ω_1 and x_1 .

We reparameterize $\Delta\omega_1$ and x_1 with a neural network with a parameter vector, θ^* , that maximizes the electrostatic energy (minimizes the free energy) and maximizes the kinetic entropy i.e.

$$x_1 = x_1(t_1, k_0; \theta^*), \quad (6)$$

$$\Delta\omega_1 = \Delta\omega_1(t_1, k_0; \theta^*). \quad (7)$$

where,

$$\theta^* = \operatorname{argmin} [U_{\text{es}}(\mathbf{p}; \theta) - \Delta\mathcal{KE}(\mathbf{p}; \theta)], \quad (8)$$

and

$$U_{\text{es}} = \sum_{t_i}^{t_f} \Delta t \sum_x \Delta x \ E^2 \quad (9)$$

$$\Delta\mathcal{KE} = \sum_{t_i}^{t_f} \Delta t \sum_x \Delta x \sum_v \Delta v \ (f \log(f) - f_{\text{MX}} \log(f_{\text{MX}})), \quad (10)$$

are the electrostatic energy, and entropy, terms in the loss function, respectively. $f_{\text{MX}} = f_{\text{MX}}(n, T)$, $n = \int f dv$, $T = \int f v^2 dv / n$, where f_{MX} is the Maxwell-Boltzmann distribution.

We vary the independent variables such that

$$k_0 \in [0.26, 0.27, \dots, 0.32], \quad (11)$$

$$t_1 \in [400, 500, \dots, 800], \quad (12)$$

giving an input space of 35 samples from which we seek to learn these functions.

We use a neural network with 2 hidden linear layers with 8 nodes activated with a ReLU function. The final layer is activated with a tanh function. The output is normalized such that $p_1 = p_{\text{norm}} \times p_{\text{out}} + p_{\text{shift}}$ where p_{out} is the output from the tanh function. We normalize the inputs between 0 and 1, and outputs with reasonable windows. For x_1 , we allow the entire domain, and $\Delta\omega_1 \in [-0.06, 0.06]$. We use the ADAM optimizer with a learning rate of 0.05.

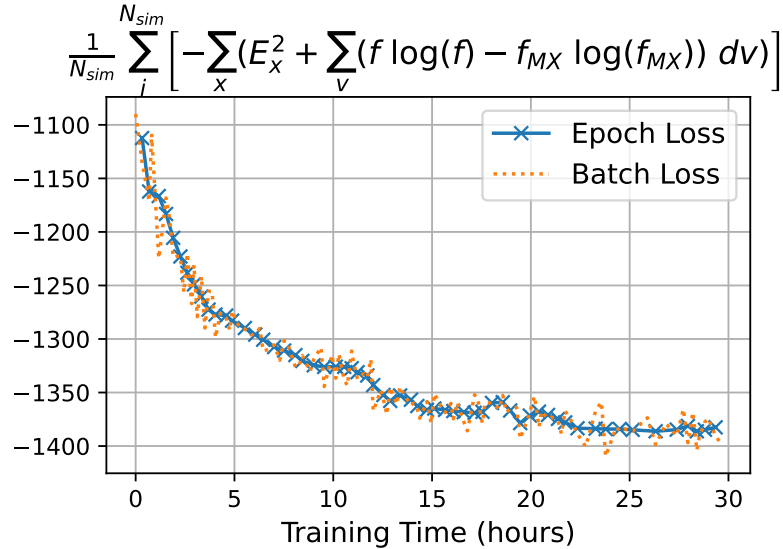


FIG. 4: The loss, a sum of eqs. 9 and 10, is plotted as a function of time. Each cross represents an epoch, and batch-wise fluctuations are also displayed. The training converges after roughly 30 hours and 2100 simulations, which amounts to 60 epochs

The training simulations are performed with $N_x = 6656, N_v = 160, N_t = 1200, t_{max} = 1100\omega_p^{-1}, x_{max} = 6600\lambda_D$. The amplitude of both drivers is 0.05. The spatial width is $400\lambda_D$ and temporal width is $50\omega_p^{-1}$.

We use a sixth order integrator in time ([23]) with operator splitting. Both operators are computed with exponential integrators with spectral discretizations in phase space ([24]). We use a spectral solver for Gauss's Law.

In order to more closely match realistic plasma conditions, we also implement a Fokker-Planck collision operator and use a non-zero collision frequency $\nu_{ee} = 10^{-4}$ for these simulations. More information on the solver is provided in the Appendix. We implement absorbing boundaries by increasing the collision frequency of the Krook operator in a small localized region at the boundary ([5]).

Figure 4 shows that the loss value is reduced over the duration of the training process, roughly 30 hours, which runs for 60 epochs. The convergence in the loss metric suggests that we were able to train a overparameterized neural network with 35 samples of data in 60 epochs. We attribute this to the effect of having so-called 'physical' gradients from training through a PDE solver ([25]).

Figure 5 shows the electric field profile for three different simulations. In fig. 5a, only

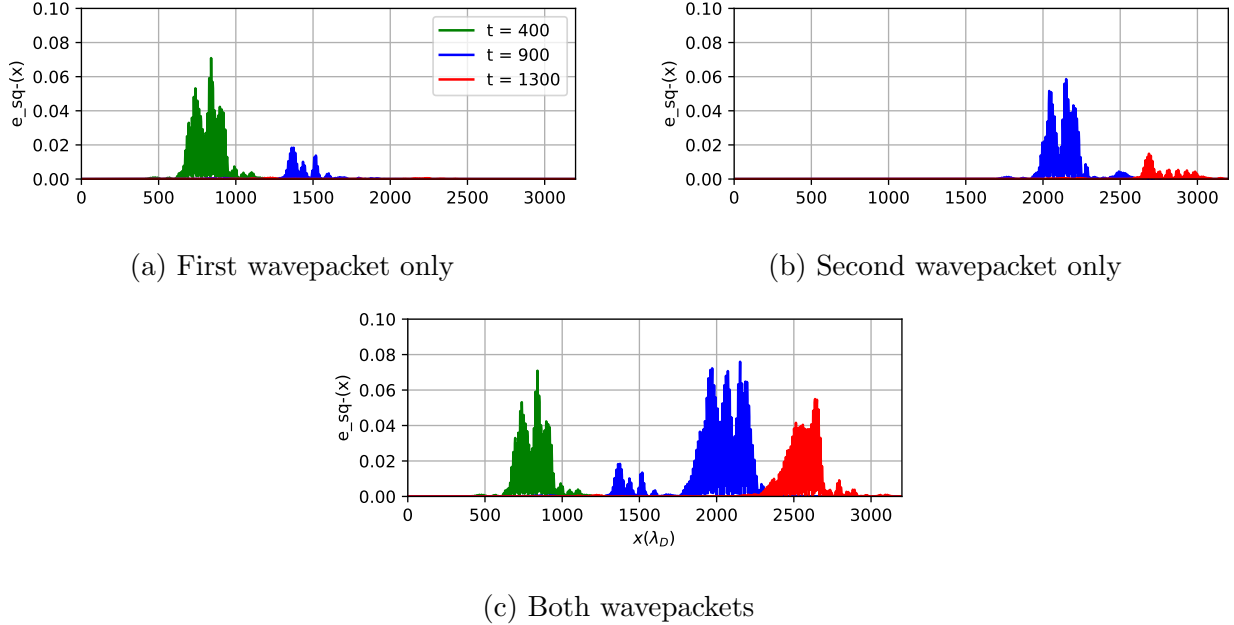


FIG. 5: Early in time (green), (c) is the same as (a). Later in time, $t = 900\omega_p^{-1}$ (blue), (a) and (c) show very similar magnitudes for the first wavepacket near $x = 1500\lambda_D$ but the second wavepacket excitation is larger in (c) than (b). At $t = 1300\omega_p^{-1}$ (red), it is clear that (c) is not a superposition of (a) and (b) because (b) has damped away, while (c) retains electrostatic energy suggesting the involvement of a superadditive process.

the first wavepacket is excited, and in fig. 5b, only the second wavepacket is excited. In fig. 5c, both wavepackets are excited. Early in time, $t = 400\omega_p^{-1}$ (green), when only the first wavepacket has been excited figs. 5a and 5c agree perfectly. The second wavepacket is excited at $t = 500\omega_p^{-1}$. At $t = 900\omega_p^{-1}$, once some time has passed after the excitation of the second wavepacket, the first wavepacket has not fully damped away. It is visible as small bumps in figs. 5a and 5c. The second wavepacket is also present at this time and easily seen in fig. 5b. A larger amplitude wavepacket is seen in fig. 5c. Late in time, the difference in amplitude between the second wavepacket in figs. 5b and 5c is obvious. The second wavepacket has nearly damped away in fig. 5b. In fig. 5c, the second wavepacket continues to persist, at nearly the same energy as it was at $t = 900\omega_p^{-1}$. We observe this superadditive behavior, where $f(x) + f(y) \leq f(x + y)$, for all wavenumbers we model.

To determine the mechanism behind this phenomenon, we turn to the phase-space dynamics. In fig. 6, (i) is a space-time plot of the electric field. The two dashed-dot red lines at the front and back of the wavepacket are parallel and indicate the velocity of the wavefront.

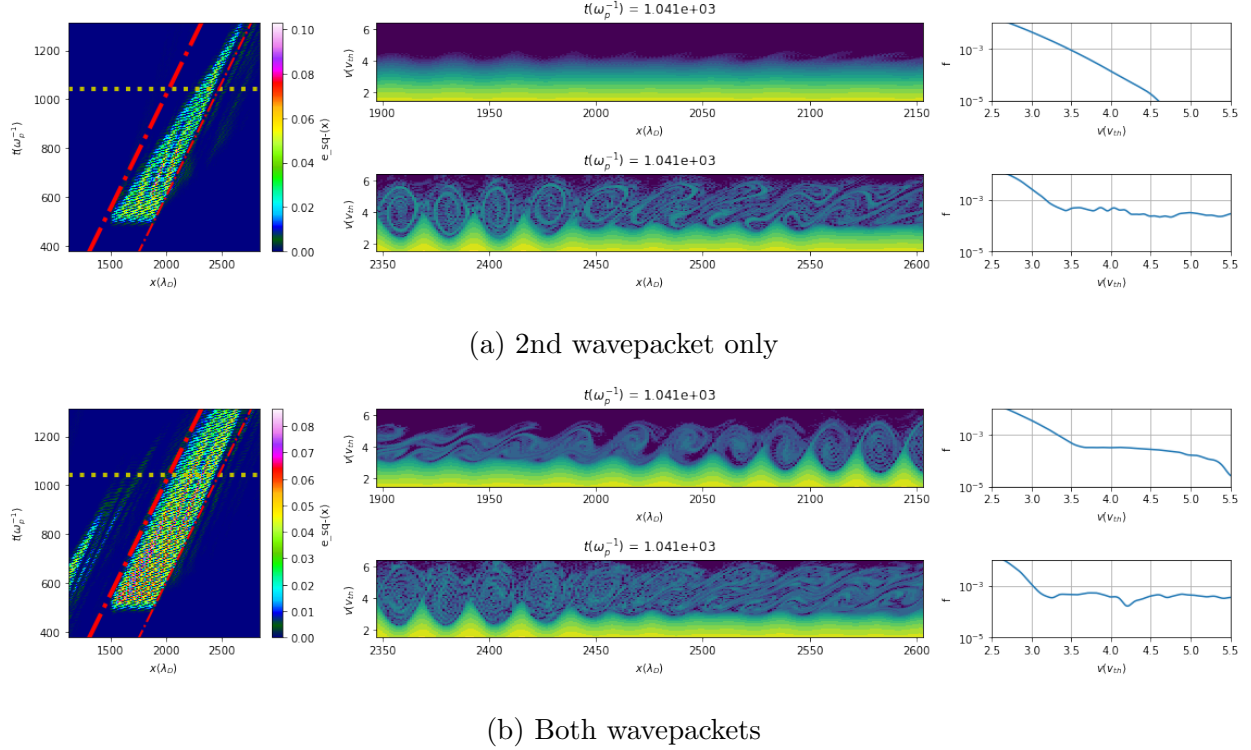


FIG. 6: **Left** - Spacetime plot of the electrostatic energy shows the long-lived wavepacket in (b) where the field in (b) survives for a longer duration than in (a). The horizontal line indicates the timestamp of the snapshots in the middle and right. The diagonal dashed-dot lines indicate the spatial location of the snapshots in the middle and right. **Middle** Phasespace plots at the back (top) and front (bottom) of the wavepacket. In (b), the phase space shows significant activity at the back of the wavepacket while in (a), the distribution function is nearly undisturbed. **Right** The spatially averaged distribution function. This confirms the fact that the distribution function has returned to a Maxwell-Boltzmann at the back of the wavepacket in (a), while in (b), the distribution function remains flat at the phase velocity of the wave. This is the reason behind the loss of damping.

In fig. 6a(i), the front of the wavepacket propagates at a seemingly faster rate than the rear. This is due to the etching effect ([6]). In fig. 6b, the wave survives for a much longer time, as was also illustrated in fig. 5.

Figure 6 (ii) and (iii) are phase-space plots with their center indicated by the intersection of the horizontal timestamp line, and the dashed-dot line at the rear wavepacket red line at the back of the wavepacket. (iv) and (v) correspond to the intersection with the dashed-

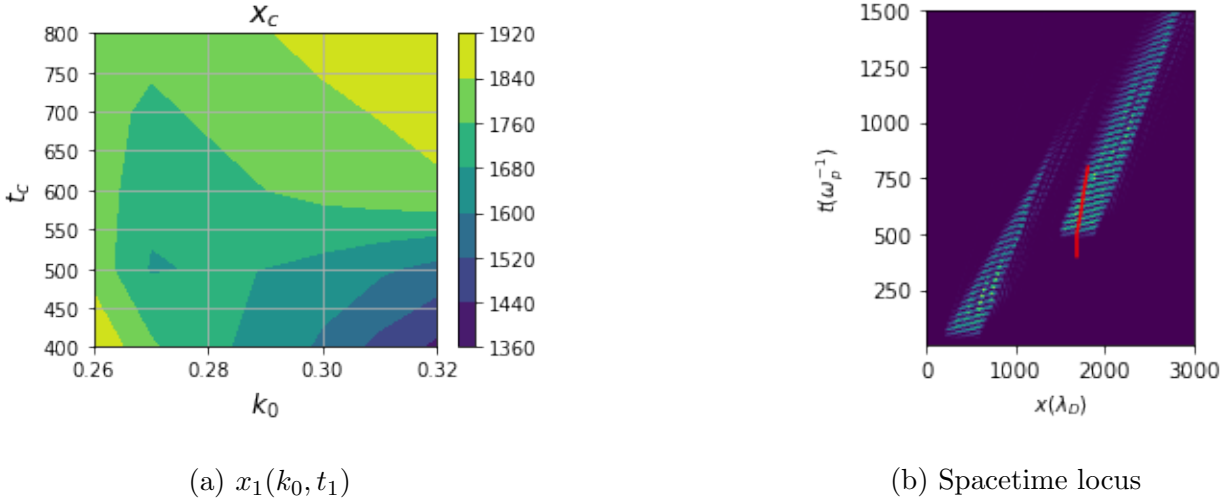


FIG. 7: (a) Learned function for the resonant spatial location as a function of wavenumber of the first wavepacket and time of excitation of the second. (b) The locus in spacetime (in red) where long-lived wavepackets can be excited for $k = 0.28$.

dot line at the front. (ii) and (iv) show the phase space within a window in x , while (iii) and (v) are the spatially averaged distribution function. (iii) and (v) serve as a proxy for approximating the propensity of Landau damping in that region. In fig. 6a(ii) and (iii), we see that the rear of the wavepacket is Maxwellian. As previously shown, this is why the rear of the wavepacket damps faster than the front as in fig. 6a(i) ([6]).

In the simulations described here, fig. 6b show that the distribution function at the back of the wavepacket has trapped particle activity (fig. 6b(ii)) and near zero slope at the phase velocity of the wave (fig. 6b(iii)). Both plots show that the slope is negligible because of the arrival of streaming detrapped particles from the first wavepacket. Due to this effect, the remergence of Landau damping that occurs due to the loss of trapped particles in isolated wavepackets no longer occurs here. This results in a reduction of the etching and the wavepacket propagates freely for some time while the particles from the first wavepacket propagate and arrive at the rear of the second wavepacket.

Figure 7 shows the results of the optimization process for the resonant spatial location. For $t_1 < 500\omega_p^{-1}$, the resonant location decreases as a function of wavenumber. From analyzing phase space, we have determined that the spatial location is related to the resonant electron transport i.e. $x_1 \approx v_{ph}t_1$. Waves with larger wavenumbers have smaller phase velocities. Because of this, the resonant spatial location decreases as a function of wavenum-

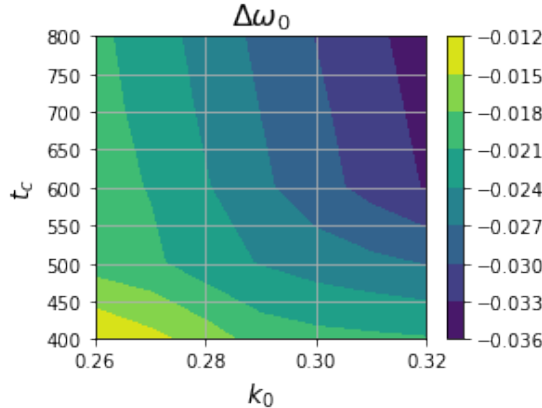


FIG. 8: The learned function for the frequency shift $\Delta\omega_1(k_0, t_1)$ as a function of wavenumber of the first wavepacket, k_0 , and time of excitation, t_1 , of the second.

ber. For a fixed wavenumber, fig. 7b shows a locus of points in space-time where long-lived wavepackets can be excited in the presence of a pre-existing wavepacket. This suggests the possibility of a critical space-time radius within which collisional relaxation has yet to occur, and non-linear effects can be exploited.

Likewise, we also learn the dependence of the optimum frequency shift as a function of k_0 and t_c , as shown in fig. 8. The learned frequency shift, a few percent here, is similar in magnitude as to that observed in previous work related to SRS ([21]). Furthermore, the frequency shift increases in magnitude as a function of wavenumber. As before, waves with larger wavenumbers have smaller phase velocities, and therefore, interact with more particles. Because of this, waves with larger wavenumbers have a larger non-linear frequency shift associated with them, as we see here ([26, 27, 28, 29]).

IV. CONCLUSION

We show how one may be able to discover novel physics using differentiable simulations by posing a physical question as an optimization problem. This required domain expertise in determining which functional dependencies to learn using neural networks.

In fig. 2, we show how one may adapt an existing computational science workflow to the autodidactic process described here. In the work performed here, this process enabled the discovery of parameters in a 4D search space with known bounds but an unknown resolution requirement. We trained the model over a coarse grid in k_0 and t_1 , and learned functions for

x_1 and ω_1 . Using gradient descent here allows an escape from the curse of dimensionality and reduces the problem from a 4D search to a 2D search + 2D gradient descent.

This discovery process is not limited to differentiable simulations. While in fig. 2, \mathcal{V} represents a PDE solve, it only needs to be a AD-enabled function that is a model for a physical system. For example, rather than a PDE solve, \mathcal{V} could represent a pre-trained neural-network-based emulator for experimental data. In such a scenario, one may be able to learn forcing function parameters for an experiment using the proposed workflow.

Finally, in neural network literature, the gradient required for the update is $\partial\mathcal{S}/\partial\theta = \partial\mathcal{S}/\partial\mathcal{G} \times \partial\mathcal{G}/\partial\theta$. We see that this is the same as eq. 3 after the addition of one more node in the computational graph for \mathcal{V} , the function that models the physical system. This allows the neural network training process to become unsupervised and data-efficient.

In future work, we aim to dive deeper into the discovered phenomenon to better understand the mechanism and derive some scalings. Reduced models of wavepacket dynamics in SRS remain useful for the development of inertial confinement fusion schemes where laser-plasma instabilities occur.

Appendix A: Simulation and Modeling details

1. Simulation Details

We reproduce the solvers and tests implemented in [24] using JAX ([30]) and Haiku ([31]) to allow the usage of automatic differentiation (AD), tactically placing neural networks, as well as the ability to run on GPU.

The validation tests cover

1. Gauss's Law
2. Landau damping
3. Density conservation of both implementations (Lenard-Bernstein and Daugherty) of the Fokker-Planck operators
4. Momentum conservation of the Daugherty implementation of the Fokker-Planck implementation

5. Energy conservation of the Lenard-Bernstein and Daugherty implementations of the Fokker-Planck operator

2. Validating the Differentiable Simulator by Recovering Known Physics

We describe an additional test here which involves recovering the linear, small-amplitude Langmuir, or electrostatic, resonance using the gradient-based implementation enabled by this AD-capable implementation. This ensures that the gradients given by the AD system are physically reasonable and are representative of physical phenomenon.

a. Electrostatic Waves

A fundamental wave in plasma physics is the electrostatic wave in unmagnetized plasmas. The dispersion relation is given in numerous textbooks, and reproduced here as

$$1 + \frac{\omega_e^2}{k^2} \int dv \frac{dg(v)/dv}{\omega - kv} = 0, \quad (\text{A1})$$

where ω_e is the plasma frequency, k is the wavenumber, ω is the resonant frequency, and v is the independent variable representing the velocity in the integral. $g(v)$ is the normalized distribution function of the plasma particles. This equation has been solved numerically and a lookup table for ω as a function of k is provided in [32].

We test the capability of our differentiable simulator framework by reproducing those calculations. To do so, we implement the functionality in fig. 2c. We choose a loss function that minimizes free energy given by

$$\mathcal{C}(\mathbf{x}_f) = - \sum_x \Delta x E(k, \omega)^2. \quad (\text{A2})$$

In this test, we launch plasma waves using a ponderomotive driver in a box with periodic boundary conditions. For each optimization, the wavenumber k and the box size x_{max} change. We provide a lower bound of 0.5 and an upper bound of 1.4 to the optimization algorithm. We use the L-BFGS algorithm implemented in SciPy ([33]). We set $f_{\text{tol}} = r_{\text{tol}} = 10^{-12}$. We learn the frequency ω that will minimize the value given by Eq. A2 and ensure that it is within 2 decimal places of the direct solution to eq. A1, which is calculated using the root finder in SciPy.

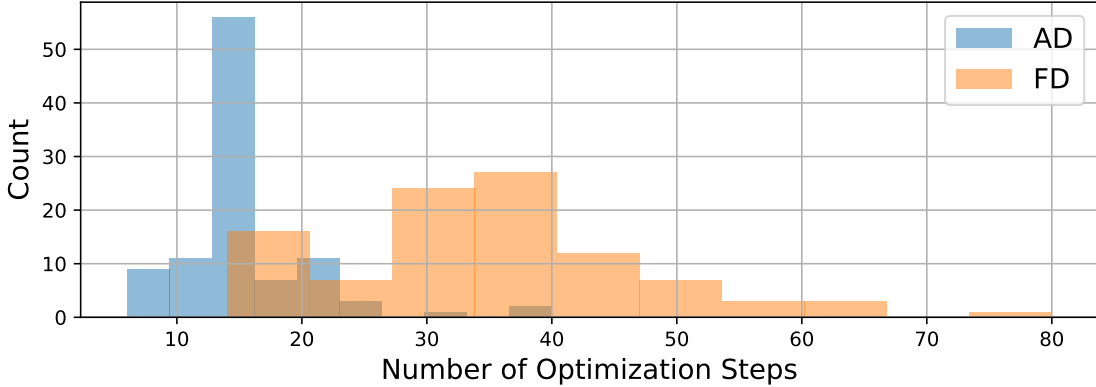


FIG. 9: We run 100 optimizations over random wavenumbers in order to quantify the performance of gradients acquired using Finite Difference (FD) and Automatic Differentiation (AD). The plot shows a comparison of the number of iterations needed to converge to a local optimum.

We optimize for the resonant frequency for 100 random wavenumbers using gradients acquired using AD and finite-difference (FD) and plot the performance. Figure 9 shows the distributions of the number of iterations required for each gradient-calculation method. We see that the finite difference method requires significantly more evaluations where the maximum number of evaluations is larger by a factor of 2. One of the optimization runs requires 80 evaluations with FD, and 40 with AD. Similarly the mean and median values are smaller by a factor of 2 for AD in comparison to those with FD. It is important to note that these results are for single-variable searches. When the dimensionality of the search space increases, using FD becomes impractical. When using neural networks that are parameterized by $\gg \mathcal{O}(10)$ parameters, using FD is simply not possible, and one must use AD to acquire gradients.

[1] J. Krall, G. Joyce, and E. Esarey, “Vlasov simulations of very-large-amplitude-wave generation in the plasma wake-field accelerator,” *Phys. Rev. A*, vol. 44, pp. 6854–6861, Nov 1991.

[2] A. G. R. Thomas, “Vlasov simulations of thermal plasma waves with relativistic phase velocity in a Lorentz boosted frame,” *Physical Review E*, vol. 94, p. 053204, Nov. 2016. Publisher: American Physical Society.

[3] C. H. K. Chen, K. G. Klein, and G. G. Howes, “Evidence for electron Landau damping in space plasma turbulence,” *Nature Communications*, vol. 10, p. 740, Feb. 2019. Number: 1 Publisher: Nature Publishing Group.

[4] O. Pezzi, G. Cozzani, F. Califano, F. Valentini, M. Guarasi, E. Camporeale, G. Brunetti, A. Retinò, and P. Veltri, “ViDA: a Vlasov–DArwin solver for plasma physics at electron scales,” *Journal of Plasma Physics*, vol. 85, p. 905850506, Oct. 2019.

[5] D. J. Strozzi, E. A. Williams, A. B. Langdon, and A. Bers, “Kinetic enhancement of Raman backscatter, and electron acoustic Thomson scatter,” *Physics of Plasmas*, vol. 14, p. 013104, Jan. 2007. arXiv: physics/0610029.

[6] J. E. Fahlen, B. J. Winjum, T. Grismayer, and W. B. Mori, “Propagation and Damping of Nonlinear Plasma Wave Packets,” *Physical Review Letters*, vol. 102, p. 245002, June 2009.

[7] J. W. Banks, R. L. Berger, S. Brunner, B. I. Cohen, and J. A. F. Hittinger, “Two-dimensional Vlasov simulation of electron plasma wave trapping, wavefront bowing, self-focusing, and sideloss,” *Physics of Plasmas*, vol. 18, no. 5, 2011. ISBN: 1070-664X.

[8] S. S. Schoenholz and E. D. Cubuk, “JAX, M.D.: End-to-End Differentiable, Hardware Accelerated, Molecular Dynamics in Pure Python,” *arXiv:1912.04232 [cond-mat, physics:physics, stat]*, Dec. 2019. arXiv: 1912.04232.

[9] Y. Bar-Sinai, S. Hoyer, J. Hickey, and M. P. Brenner, “Learning data-driven discretizations for partial differential equations,” *Proceedings of the National Academy of Sciences*, vol. 116, pp. 15344–15349, July 2019. Publisher: National Academy of Sciences Section: Physical Sciences.

[10] J. Zhuang, D. Kochkov, Y. Bar-Sinai, M. P. Brenner, and S. Hoyer, “Learned discretizations for passive scalar advection in a 2-D turbulent flow,” *arXiv:2004.05477 [cond-mat, physics:physics]*, Nov. 2020. arXiv: 2004.05477.

[11] D. Kochkov, J. A. Smith, A. Alieva, Q. Wang, M. P. Brenner, and S. Hoyer, “Machine learning accelerated computational fluid dynamics,” *arXiv:2102.01010 [physics]*, Jan. 2021. arXiv: 2102.01010.

[12] P. Holl, V. Koltun, and N. Thuerey, “Learning to Control PDEs with Differentiable Physics,” *arXiv:2001.07457 [physics, stat]*, Jan. 2020. arXiv: 2001.07457.

[13] T. Antonsen, E. J. Paul, and M. Landreman, “Adjoint approach to calculating shape gradients for three-dimensional magnetic confinement equilibria,” *Journal of Plasma Physics*, vol. 85,

Apr. 2019. Publisher: Cambridge University Press.

- [14] E. J. Paul, T. Antonsen, M. Landreman, and W. A. Cooper, “Adjoint approach to calculating shape gradients for three-dimensional magnetic confinement equilibria. Part 2. Applications,” *Journal of Plasma Physics*, vol. 86, Feb. 2020. Publisher: Cambridge University Press.
- [15] E. J. Paul, M. Landreman, and T. Antonsen, “Gradient-based optimization of 3D MHD equilibria,” *Journal of Plasma Physics*, vol. 87, Apr. 2021. Publisher: Cambridge University Press.
- [16] C. Zhu, S. R. Hudson, Y. Song, and Y. Wan, “New method to design stellarator coils without the winding surface,” *Nuclear Fusion*, vol. 58, p. 016008, Nov. 2017. Publisher: IOP Publishing.
- [17] N. McGreivy, S. R. Hudson, and C. Zhu, “Optimized finite-build stellarator coils using automatic differentiation,” *Nuclear Fusion*, vol. 61, p. 026020, Jan. 2021. Publisher: IOP Publishing.
- [18] J. Nocedal and S. J. Wright, *Numerical Optimization*. New York, NY, USA: Springer, 2e ed., 2006.
- [19] I. B. Bernstein, J. M. Greene, and M. D. Kruskal, “Exact nonlinear plasma oscillations,” *Phys. Rev.*, vol. 108, pp. 546–550, Nov 1957.
- [20] T. O’Neil, “Collisionless Damping of Nonlinear Plasma Oscillations,” *Physics of Fluids*, vol. 8, no. 12, p. 2255, 1965. arXiv: 1011.1669v3 ISBN: 9788578110796.
- [21] I. N. Ellis, D. J. Strozzi, B. J. Winjum, F. S. Tsung, T. Grismayer, W. B. Mori, J. E. Fahlen, and E. A. Williams, “Convective Raman amplification of light pulses causing kinetic inflation in inertial fusion plasmas,” *Physics of Plasmas*, vol. 19, p. 112704, Nov. 2012. Publisher: American Institute of Physics.
- [22] B. J. Winjum, A. Tableman, F. S. Tsung, and W. B. Mori, “Interactions of laser speckles due to kinetic stimulated Raman scattering,” *Physics of Plasmas*, vol. 26, p. 112701, Nov. 2019. Publisher: American Institute of Physics.
- [23] F. Casas, N. Crouseilles, E. Faou, and M. Mehrenberger, “High-order Hamiltonian splitting for the Vlasov–Poisson equations,” *Numerische Mathematik*, vol. 135, no. 3, pp. 769–801, 2017. arXiv: 1510.01841 Publisher: Springer Berlin Heidelberg.
- [24] A. Joglekar and M. Levy, “VlaPy: A Python package for Eulerian Vlasov-Poisson-Fokker-Planck Simulations,” *Journal of Open Source Software*, vol. 5, p. 2182, Sept. 2020.

[25] P. Holl, V. Koltun, and N. Thuerey, “Physical Gradients for Deep Learning,” *arXiv:2109.15048 [physics]*, Oct. 2021. arXiv: 2109.15048.

[26] W. M. Manheimer and R. W. Flynn, “Formation of Stationary Large Amplitude Waves in Plasmas,” *The Physics of Fluids*, vol. 14, pp. 2393–2396, Nov. 1971.

[27] R. L. Dewar, “Frequency Shift Due to Trapped Particles,” *The Physics of Fluids*, vol. 15, pp. 712–714, Apr. 1972.

[28] G. J. Morales and T. M. O’Neil, “Nonlinear frequency shift of an electron plasma wave,” *Physical Review Letters*, vol. 28, no. 7, pp. 417–420, 1972.

[29] R. L. Berger, S. Brunner, T. Chapman, L. Divol, C. H. Still, and E. J. Valeo, “Electron and ion kinetic effects on non-linearly driven electron plasma and ion acoustic waves,” *Physics of Plasmas*, vol. 20, p. 032107, Mar. 2013.

[30] J. Bradbury, R. Frostig, P. Hawkins, M. J. Johnson, C. Leary, D. Maclaurin, G. Necula, A. Paszke, J. VanderPlas, S. Wanderman-Milne, and Q. Zhang, “JAX: Autograd and XLA,” 2018. original-date: 2018-10-25T21:25:02Z.

[31] T. Hennigan, T. Cai, T. Norman, and I. Babuschkin, “Haiku: Sonnet for JAX,” 2020. original-date: 2020-02-18T07:14:02Z.

[32] J. Canosa, “Numerical solution of Landau’s dispersion equation,” *Journal of Computational Physics*, vol. 13, pp. 158–160, Sept. 1973.

[33] SciPy 1.0 Contributors, P. Virtanen, R. Gommers, T. E. Oliphant, M. Haberland, T. Reddy, D. Cournapeau, E. Burovski, P. Peterson, W. Weckesser, J. Bright, S. J. van der Walt, M. Brett, J. Wilson, K. J. Millman, N. Mayorov, A. R. J. Nelson, E. Jones, R. Kern, E. Larson, C. J. Carey, I. Polat, Y. Feng, E. W. Moore, J. VanderPlas, D. Laxalde, J. Perktold, R. Cimrman, I. Henriksen, E. A. Quintero, C. R. Harris, A. M. Archibald, A. H. Ribeiro, F. Pedregosa, and P. van Mulbregt, “SciPy 1.0: fundamental algorithms for scientific computing in Python,” *Nature Methods*, vol. 17, pp. 261–272, Mar. 2020.